Journal of
Applied Crystallography
ISSN 0021-8898

Received 14 August 2006
Accepted 11 January 2007

Anomalous small- and wide-angle X-ray scattering and X-ray absorption spectroscopy for Pt and Pt–Ru nanoparticles

U-Ser Jeng,* Ying-Huang Lai, Hwo-Shuenn Sheu, Jyh-Fu Lee, Ya-Sen Sun, Wei-Tsung Chuang, Yu-Shan Huang and Din-Goa Liu

National Synchrotron Radiation Research Center, 101 Hsin-Ann Road, Hsinchu Science Park, Hsinchu 30076, Taiwan. Correspondence e-mail: usjeng@nsrrc.org.tw

We have characterized the structures of two kinds of catalytic nanoparticles of Pt and Pt–Ru, using anomalous small-angle X-ray scattering (ASAXS), anomalous wide-angle X-ray scattering (AWAXS) and extended X-ray absorption fine structure (EXAFS) spectroscopy. With several X-ray energies near the Pt L_{III} edge, the AWAXS data reveal a face-centered cubic (f.c.c.) crystalline structure for Pt nanoparticles supported on carbon black, whereas the ASAXS data characterize the monometallic nanoparticles as polydisperse spheres with a mean size of 23 Å and a size distribution of 20%. With similar X-ray energies, ASAXS and AWAXS data for the Pt–Ru nanoparticles indicate that they have a mean size of ~29 Å and a slightly Pt-rich core that can be characterized by an f.c.c. crystalline structure similar to that of the pure Pt nanoparticles. The coordination numbers of the bimetallic nanoparticles extracted from the EXAFS data, collected at the Pt L_{III} edge and Ru K edge, also reveal a consistent structure of largely, but not completely, intermixed Pt and Ru atoms in the nanoparticles.

1. Introduction

The potential of polymeric electrolyte-membrane fuel cells (PEMFC) as a clean and mobile power source has attracted much attention for some time. Nevertheless, there are issues that need to be resolved before practical use of the cells. For instance, in the development of direct methanol fuel cells (DMFC) (McNicol *et al.*, 1999), CO poisoning on the Pt-catalyst based anodes causes a serious deterioration in converting chemical energy into electrical energy. One of the solutions involves the replacement of pure Pt catalysts by Pt–Ru bimetallic catalysts for on-site recovering of the CO-poisoned Pt atoms, *via* an oxidative removal of CO by oxygen-like species adsorbed on adjacent Ru atoms. Obviously, surface modification becomes crucial in improving the catalytic performance of bimetallic catalysts.

To extract details of the structure and structural changes of embedded monometallic or bimetallic catalyst nanoparticles, including shape, size, crystalline structure and atomic distribution, during the process of, for instance, thermal annealing or electrochemical reduction, anomalous small-angle X-ray scattering (ASAXS) and anomalous wide-angle X-ray scattering (AWAXS) have been shown to be effective methods (Haubold *et al.*, 1997, 2003; Bazin *et al.*, 1997; Adora *et al.*, 2004), due to the selective sensitivity of the probes to the individual components (atoms) of the nanoparticles, when X-ray energy is tuned close to the characteristic absorption edge of the atoms in the nanoparticles. Furthermore, the complementary technique of X-ray absorption spectroscopy (XAS) can provide the local atomic structure of the nanoparticles from extended X-ray absorption fine structure (EXAFS) (Liu *et al.*, 2005). Combining the scattering tools and EXAFS, all based on X-ray resonance, one can obtain integrated structural information for the catalyst nanoparticles of interest, as demonstrated in several reports (Bazin *et al.*, 1997, 2002; Vad *et al.*, 2002; Brumberger *et al.*, 2005). In this study, we apply ASAXS, AWAXS and EXAFS to characterize the structures of the two kinds of catalyst nanoparticles, Pt nanoparticles supported on carbon black and Pt–Ru nanoparticles without the support of carbon black. Utilizing the anomalous dispersion near the Pt L_{III} edge, we obtain information on the Pt distribution inside the Pt–Ru nanoparticles.

2. Anomalous X-ray scattering

For monometallic nanoparticles, AWAXS intensity is related to the complex atomic scattering factor

$$f(Q, E) = f_o(Q) + f'(E) + if''(E), \quad (1)$$

with the modulus of the scattering vector $Q = 4\pi\sin\theta/\lambda$ defined by the scattering angle 2θ and the wavelength λ (or energy E) of the X-rays. The first term in equation (1) is energy-independent and corresponds to the number of electrons when $Q = 0$, whereas the second and third terms are anomalous dispersion corrections (Bazin *et al.*, 1997; Vad *et al.*, 2002). The ratio of the AWAXS peak intensities at two energies E_1 and E_2 can be conveniently expressed as:

$$R_w = |f_{E_2}|^2/|f_{E_1}|^2 = (f_r^2 + f''^2)_{E_2}/(f_r^2 + f''^2)_{E_1}, \quad (2)$$

with the real part $f_r(Q, E) = f_o(Q) + f'(E)$.

For polydisperse nanoparticles with random distribution, the interference between the particles can be neglected, and the corre-

sponding small-angle X-ray scattering (SAXS) profile as a function of Q can be expressed as

$$I(Q) = <n_p> \int P(Q, r) f(r) \mathrm{d}r. \quad (3)$$

Here, $n_p(r) = <n_p> f(r)$ is the number density of particles of size r, with $<n_p>$ representing the mean number density and $f(r)$ the normalized size-distribution function, for instance the often-used Schultz distribution (Jeng *et al.*, 2004). For spherical Pt nanoparticles, the form factor $P(Q,r) = |\Delta\rho V_p(3j_1(Qr)/Qr)|^2$, where $\Delta\rho$ is the scattering contrast between the particles and the matrix, of scattering length density ρ and ρ_o, respectively. V_p is the particle volume and j_1 the first-order spherical Bessel function. For a one-phase system, the SAXS intensity, but not the profile, can be affected by the anomalous X-ray dispersion of the system, and the ratio of the two SAXS intensities measured at the two energies E_1 and E_2 may be written as

$$R_s = \frac{\left|\rho_{E_2} - \rho_o\right|^2}{\left|\rho_{E_1} - \rho_o\right|^2} \approx R_w \left[1 - 2\rho_o \left(\frac{1}{\rho_{E_2}} - \frac{1}{\rho_{E_1}}\right)\right], \quad \text{with} \quad \rho_{E_1} \gg \rho_o. \quad (4)$$

In the above equation, with $\rho_o = 0$ (nanoparticles without supporting matrix), R_s reduces to R_w. Here, we have neglected the small correction by f'' (less than one percent in our case). For Pt nanoparticles supported on carbon black, we have two possible interfaces, Pt–C and Pt–porosity(air). Since the scattering length density of Pt is much larger than that of the carbon black used ($\rho_o = 15.3 \times 10^{-6}$ Å^{-2}), we may conveniently neglect the difference between the two contrasts of the Pt–C and Pt–air interfaces, which leads to $R_s \sim R_w$ (see equation 4). For example, when E_1 and E_2 are, respectively, 10.353 and 11.548 keV, we have $\rho_{\text{Pt-}E_1} = 131.5 \times 10^{-6}$ Å^{-2} and $\rho_{\text{Pt-}E_2} = 115.1 \times 10^{-6}$ Å^{-2}, which values lead to $R_s = 0.74$ for Pt nanoparticles fully embedded in carbon grains, and $R_s = 0.77$ for nanoparticles fully emerging from the carbon grains. Note that in equation (4), we have assumed that the energy-independent scattering contribution from the porosity/carbon interfaces is removed (which can be done by taking the difference of the two ASAXS intensities measured at E_1 and E_2).

For single-phase bimetallic nanoparticles of A and B atoms, with mean scattering length density $\rho = \chi\rho_A + (1 - \chi)\rho_B$, the anomalous dispersion changes the SAXS intensity but not the SAXS profile of the nanoparticles. Thus, it is possible to extract the atomic fraction χ of A, or $(1 - \chi)$ of B, using R_s extracted from the two ASAXS intensities measured at two energies E_1 and E_2, *via* the relation

$$\chi = \frac{\rho_{B,E_2} - \sqrt{R_s}\rho_{B,E_1}}{\sqrt{R_s}(\Delta\rho_{AB})_{E_1} - (\Delta\rho_{AB})_{E_2}}, \quad (5)$$

derived on the basis of equation (4), with $\Delta\rho_{AB} = \rho_A - \rho_B$.

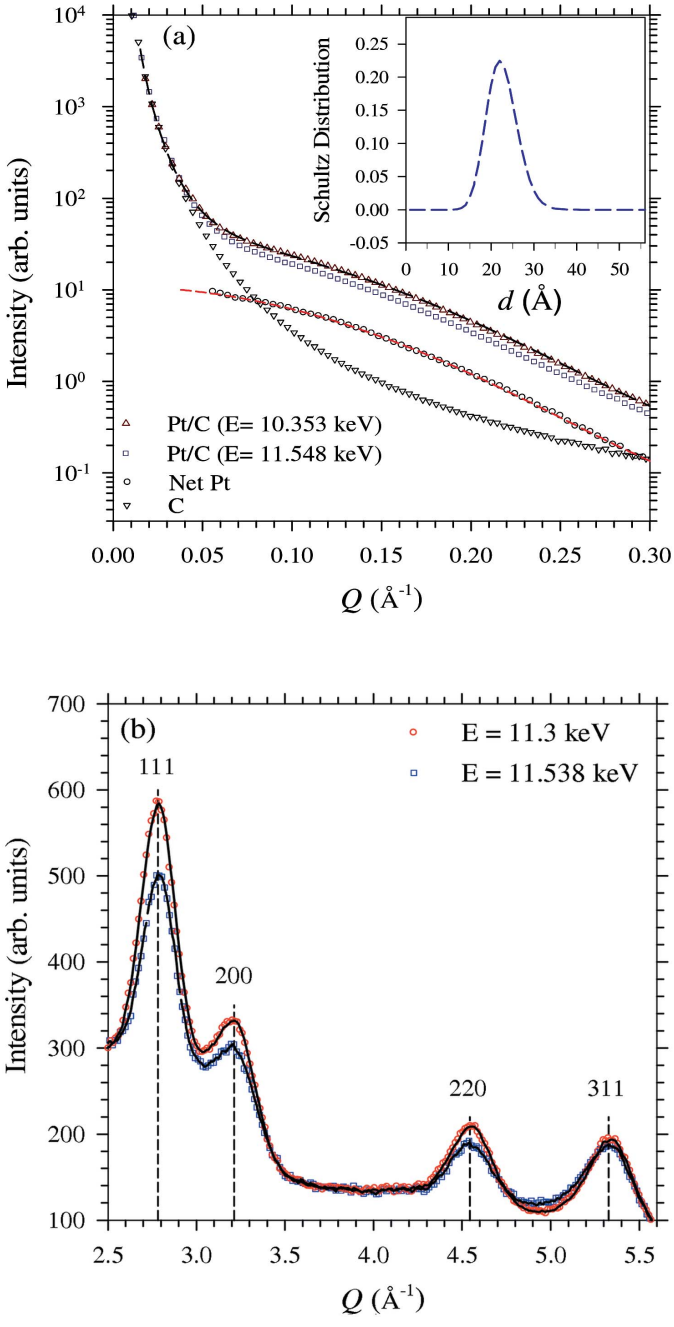

Figure 1
(*a*) The SAXS profiles measured for Pt/C and carbon black. The net scattering profile $I(Q)_{Pt}$ for the Pt nanoparticles (circles) is fitted (short-dashed curve) with polydisperse spheres of a Schultz distribution, as shown in the inset. A simulation (long-dashed curve), taking into account the scattering contributions of the carbon black and Pt nanoparticles, is also given for the SAXS data measured at E = 10.353 keV. (*b*) AWAXS data collected for the Pt/C system. The four dotted lines indicate the four f.c.c. peaks of bulk Pt.

3. Materials and methods

Pt nanoparticles supported on carbon black (Cabot Vulcan XC-72R) and pure Pt–Ru nanoparticles (free of supporting matrix), were received from E-TEK Inc. and Johnson–Matthey Co., respectively. The bimetallic nanoparticles have a nominal atomic fraction of Pt–50 at.% Ru. For the Pt nanoparticles, ASAXS experiments were performed on a SAXS setup at the BL01B endstation of the National Synchrotron Radiation Research Center (NSRRC), Taiwan. The details of the instrumental setup were reported previously (Lai *et al.*, 2005). The AWAXS data were collected at the powder X-ray diffraction endstation at BL01C2 of the NSRRC. For the Pt–Ru nanoparticles, the ASAXS and AWAXS data were collected simultaneously using the small- and wide-angle X-ray scattering (SWAXS) instrument at BL17B3 of the NSRRC, with several beam energies near the Pt L_{III} edge (11.564 keV). For differentiating the variation of scattering intensity due to the change of X-ray energy, instrument calibration for scattering intensity and Q is essential, in addition to rigorous data corrections for electronic noise of the detector, background scattering, incoming flux, the angle-dependent path length of

X-rays in the sample, and detector pixel sensitivity, as detailed in a previous report (Lai *et al.*, 2006).

X-ray absorption spectra for the Pt and Pt–Ru nanoparticles were recorded, in transmission mode, at the Pt L_{III} edge and Ru K edge at the beamlines 17C1 and 01C1 of the NSRRC, using gas-filled ionization chambers. Energy was scanned from 200 eV below to 1000 eV above the X-ray absorption edges (Liu *et al.*, 2005).

4. Results and discussion

4.1. Pt nanoparticles embedded in carbon black

Fig. 1(*a*) shows the ASAXS data for Pt nanoparticles supported on carbon black measured at two beam energies, E = 10.353 keV (off resonance) and E = 11.548 keV (near resonance). For comparison, the SAXS profile for pure carbon black was also measured. The good overlap of the SAXS profiles in the lower-Q region ($Q \leq 0.03$ Å^{-1}) indicates that the carbon black dominates the energy-independent scattering in this region. The SAXS of the carbon black of a power-law scattering characteristic [$I(Q) \propto Q^{-3.9}$], however, contributes much less than that of the Pt nanoparticles in the intermediate to high-Q region (> 0.07 Å^{-1}). In this region, the ASAXS profile measured for Pt–C at E = 10.353 keV overlaps well with that measured at 11.548 keV, after the former has been scaled down in intensity by a factor of 0.77 (within a range of ±0.01). The intensity reduction factor is consistent with R_s = 0.77 calculated previously for the case of Pt nanoparticles emerging from the carbon grains. As a comparison, R_s is 0.74 for fully embedded Pt nanoparticles. Using $I(Q)_{Pt} = I(Q,E)_{10.352\ keV} - I(Q,E)_{11.548\ keV}$, we can remove the energy-independent scattering contribution of the carbon black. The $I(Q)_{Pt}$ profile thus obtained contains only the scattering contribution of the Pt nanoparticles, and can be well described (dashed curve in Fig. 1*a*) by a model calculation using polydisperse spheres of a Schultz size distribution. The fitted mean size for the Pt nanoparticles is 23.3±0.6 Å, with a polydispersity of ~25% (inset of Fig. 1*a*).

The wide-angle X-ray scattering (WAXS) data measured for the Pt nanoparticles (Fig. 1*b*) exhibit characteristic peaks of a face-centered cubic (f.c.c.) structure. The first two diffraction peaks, 111 and 200, were each subject to an intensity drop of 13±2% when the beam energy was changed from 11.3 keV to 11.538 keV. These values are slightly smaller than the values of 16% and 17% calculated using equation (2) with the corresponding $f_r(Q,E)$ values. Here, we neglect the other two peaks, 220 and 311, of weaker scattering intensities (worse signal-to-noise ratios). The lattice constant of 3.915 Å extracted from the diffraction peaks of the Pt nanoparticles is very close to the value of 3.920 Å in bulk Pt. The mean crystalline size (22.7±0.5 Å) estimated from the peak widths using the Scherrer equation matches the mean size (23.2±0.5 Å) given by ASAXS, indicating high crystallinity of the Pt nanoparticles.

4.2. Pt–Ru nanoparticles

For pure Pt–Ru nanoparticles with no supporting matrix of carbon black, the AWAXS data measured at E = 11.0, 11.3 and 11.548 keV near the L_{III} edge of Pt (Fig. 2) exhibit two characteristic f.c.c. peaks similar to those of the Pt nanoparticles shown previously. The 111 peak centered at Q = 2.81±0.01 Å^{-1} is in between those for bulk Pt (Q = 2.782 Å^{-1}) and Ru (Q = 2.848 Å^{-1}). Assuming that Vegard's law can be applied in this case, the observed peak position corresponds to an f.c.c. solid solution of a Pt atomic fraction of 60±10%. The mean crystalline size estimated from the peak width using the Scherrer equation is 25.7±0.5 Å. On the other hand, using the peak intensity ratio of 0.82 of the two 111 peaks measured at E = 11.0 keV and 11.548 keV, we have also extracted a consistent Pt content of 63±10% for the crystalline phase of the nanoparticles, on the basis of equations (2) and (5).

In Fig. 3, we show the $R_s(Q)$ profiles (see equation 4) obtained by dividing the ASAXS profiles measured at E = 11.3 and 11.548 keV by the profile measured at 11.0 keV. For the case of E = 11.3 keV, the $R_s(Q)$ profile is essentially flat with a magnitude close to unity, indicating that there is little X-ray anomalous dispersion in the

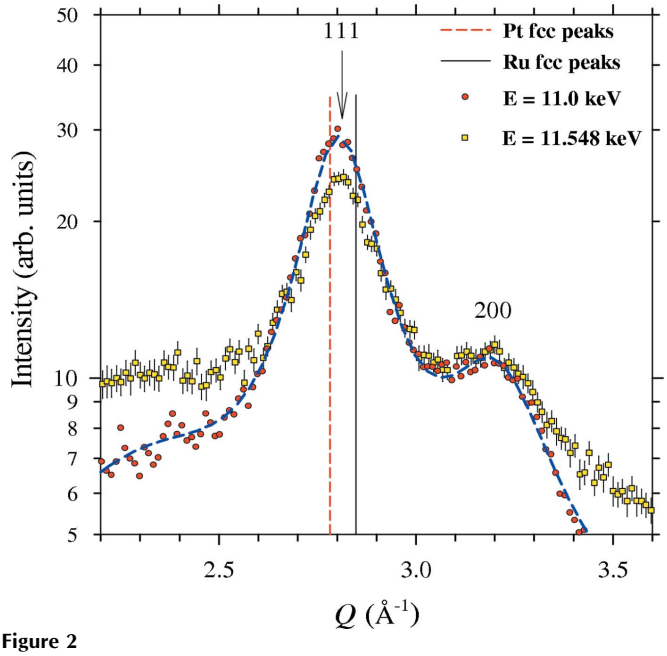

Figure 2
AWAXS data for the Pt–Ru nanoparticles collected near the Pt L_{III} edge. Also shown are the f.c.c. peak positions of bulk Pt (dashed line) and bulk Ru (solid line). The data collected at E = 11.3 keV, overlapping well with those collected at E = 11.0 keV, have been omitted for clarity.

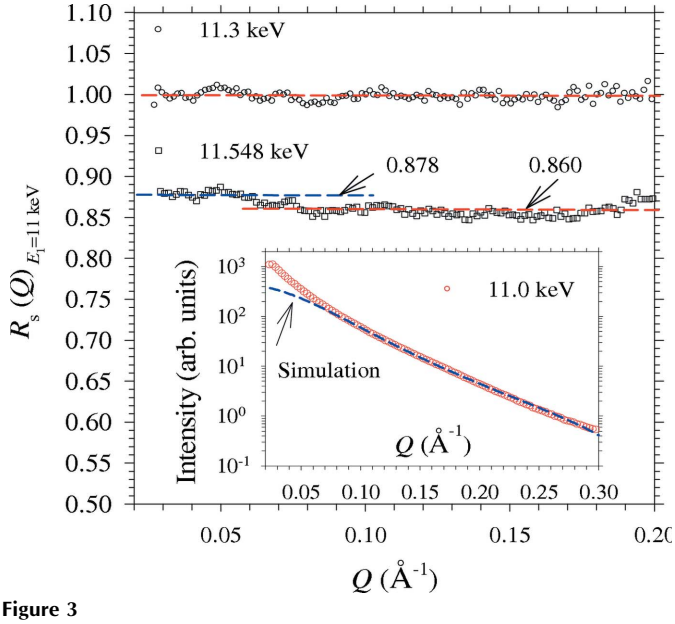

Figure 3
$R_s(Q)$ profiles obtained by dividing ASAXS data measured at E = 11.3 and 11.548 keV by that measured at 11.0 keV. The inset shows the SAXS profile measured at 11.0 keV, fitted with a model calculation for polydisperse spheres of a mean size of 29 Å and a polydispersity of 25%.

Table 1
Structural parameters derived from the EXAFS data for the Pt–Ru nanoparticles, where N is the coordination number, R is the interatomic distance and σ^2 (obtained from the Debye–Waller factor) is the mean-squared deviation of R.

	Bond	N	R (Å)	σ^2 (Å^2)
Pt L_{III} edge	Pt—Ru	3.4±0.4	2.710±0.007	0.0054±0.001
	Pt—Pt	5.1±0.1	2.730±0.006	0.0055±0.0005
Ru K edge	Ru—Ru	2.7±0.5	2.650±0.013	0.0063±0.002
	Ru—Pt	3.4±1.0	2.710±0.007	0.0056±0.002

energy range. On the other hand, for the case of E = 11.548 keV, the $R_s(Q)$ profile obtained can be characterized by two constants significantly smaller than unity, 0.878 in the low-Q region and 0.860 in the high-Q region. The close but different $R_s(Q)$ values indicate largely uniformly distributed Pt atoms inside the Pt–Ru nanoparticles, with a slightly higher Pt atomic fraction in the core area (which dominates the anomalous scattering intensity change in the high-Q region). Using equation (5) with R_s = 0.860 extracted in the high-Q region, ρ = 128.2 and 115.1 × 10^{-6} Å^{-2} for Pt at E = 11.0 and 11.548 keV, respectively, and 90.4 × 10^{-6} Å^{-2} for Ru at either of the two X-ray energies, we can extract a Pt atomic fraction of 64±5% for the core area of the nanoparticle. Similarly, we can also obtain a Pt atomic fraction of 53±5% from R_s = 0.878 extracted in the low-Q region, where the anomalous scattering intensity change is dominated by the Pt atomic fraction of the whole nanoparticle.

With the same model as that used previously for the Pt nanoparticles, we fitted the SAXS data measured at E = 11.0 keV (dashed curve in the inset of Fig. 3) with polydisperse spheres of a mean size of 29 Å and a polydispersity of 25%. In the Q-range lower than ~0.09 Å^{-1}, the simulation, containing only individual particle scattering, gradually falls below the data as Q decreases. The excess scattering is presumably contributed by the aggregation of the particles, and can be fitted by the Debye–Buche equation (Debye *et al.*, 1957), with a correlation length ξ = 26 Å (corresponding to a cluster size 2ξ ~ 52 Å).

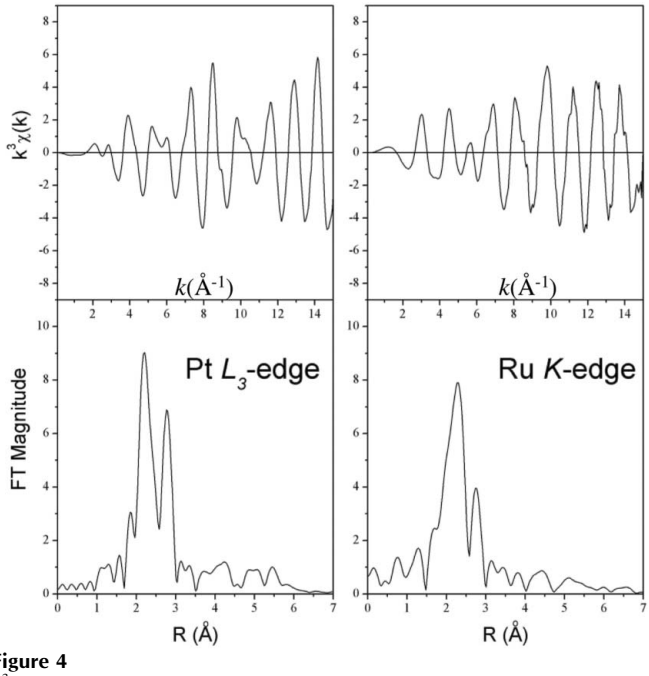

Figure 4
k^3-weighted EXAFS data (above) and the corresponding Fourier transform (without phase correction) for the radial distribution functions (below), at the Pt L_{III} edge and Ru K edge, for the pure Pt–Ru nanoparticles after reduction by hydrogen at 303 K.

For local structural information, Fig. 4 presents the k^3-weighted EXAFS data (k, defined by $2\pi/\lambda$, is the modulus of the wave vector of the X-rays) and the corresponding radial distribution functions of the Pt and Ru atoms of the Pt–Ru nanoparticles after reduction by hydrogen at 303 K. Detailed structural parameters obtained from the EXAFS data analysis, including the coordination number N and the interatomic distance R, are summarized in Table 1. The difference in the coordination numbers of Pt and Ru indicates that Pt is surrounded by more Pt atoms (N_{Pt-Pt} = 5.1) than Ru atoms (N_{Pt-Ru} = 3.4), whereas Ru shows little preference in neighboring atoms (N_{Ru-Ru} ~ N_{Ru-Pt}). Compared with the Pt–Ru nanoparticles embedded in carbon black (Pt–Ru/C) that we studied previously (Liu *et al.*, 2005), having N_{Ru-Ru} (5.3) >> N_{Ru-Pt} (1.9) and N_{Pt-Pt} (7.7) >> N_{Pt-Ru} (1.9) for a clearer core–shell characteristic (better Pt–Ru phase separation), the coordination numbers obtained here for pure Pt–Ru nanoparticles suggest that the Pt and Ru atoms are relatively well mixed in the nanoparticles. Note that the measured coordination number N_{Pt-Pt} = 8.3 for the pure Pt nanoparticles may be used as a reference for the degree of phase separation of Pt in the Pt–Ru nanoparticles. Furthermore, the reduced N_{Pt-Pt}, together with the increased N_{Pt-Ru} for pure Pt–Ru nanoparticles, leads to a smaller mean bond distance R than that for the Pt–Ru/C nanoparticles (of a crystalline Pt core). This result is also consistent with the f.c.c. solid solution structure, with a smaller lattice constant than that of pure Pt, revealed by the previous AWAXS data for pure Pt–Ru nanoparticles.

5. Conclusions

The ASAXS, AWAXS and EXAFS results have provided consistent and complementary structure information for the catalyst nanoparticles studied. The carbon black supported Pt nanoparticles, of a mean size of 22 Å, are nearly 100% crystallized and are well dispersed in the carbon black matrix without clustering or aggregation. On the other hand, the Pt–Ru nanoparticles without a supporting matrix have a mean size of ~29 Å and a structure of largely intermixed Pt and Ru atoms. In a more detailed picture, the Pt–Ru nanoparticles contain an f.c.c. crystalline core, with a core composition slightly in favor of Pt.

We thank Mr. J.-M. Lin for assisting with the ASAXS data collection. This work was partially supported by the NSC under grant No. NSC-94-2112-M-213-011.

References

Adora, S., Simon, J. P., Soldo-Olivier, Y., Faure, R., Chainet, E. & Durand, R. (2004). *Chem. Phys. Chem.* **5**, 1178–1184.
Bazin, D. C., Sayers, D. A., & Rehr, J. J. (1997). *J. Phys. Chem. B*, **101**, 11040–11050.
Bazin, D., Guczi, L. & Lynch, J. (2002). *J. Catal. A*, **226**, 87–113.
Brumberger, H., Hagrman, D., Goodisman, J. & Finkelstein, K. D. (2005). *J. Appl. Phys.* **38**, 147–151, 324–332.

Debye, P., Anderson, H.R. Jr & H. Brumberger (1957). *J. Appl. Phys.* **28**, 679–683.
Haubold, H.-G., Vad, T., Waldöfner, N. & Bönnemann, H. (2003). *J. Appl. Cryst.* **36**, 617–620.
Haubold, H.-G. & Wang, X. H. (1995). *Nucl. Instrum. Methods Phys. Res. B*, **97**, 50–54.
Haubold, H.-G., Wang, X. H., Goerigk, G. & Schilling, W. (1997). *J. Appl. Cryst.* **30**, 653–658.
Jeng, U., Sun, Y. S., Lee, H.-Y., Hsu, C.-H., Liang, K. S., Yeh, S.-W. & Wei, K.-H. (2004). *Macromolecules*, **37**, 4617–4622.
Lai, Y. H., Sun, Y. S., Jeng, U., Lin, J. M., Lin, T.-L., Sheu, H.-S., Chuang, W.-T., Huang, Y.-S., Hsu, C.-H., Lee, M.-T., Lee, H.-Y., Liang, K. S., Gabriel, A. & Koch, M. H. J. (2006). *J. Appl. Cryst.* **39**, 871–877.
Lai, Y. H., Sun, Y. S., Jeng, U., Song, Y. F., Tsang, K. L. & Liang, K. S. (2005). *Nucl. Instrum. Methods Phys. Res. B*, **238**, 205–213.
Liu, D.-G., Lee, J.-F. & Tang, M.-T. (2005). *J. Mol. Catal. A*, **240**, 197–206.
McNicol, B. D., Rand, D. A. J. & Williams, K. R. (1999). *J. Power Sources*, **83**, 15–31.
Vad, T., Haubold, H.-G., Waldöfner, N. & Bönnemann, H. (2002). *J. Appl. Cryst.* **35**, 459–470.